

1D Probabilistic Undersampling Pattern Optimization for MR Image Reconstruction

Shengke Xue, Xinyu Jin, and Ruiliang Bai

Abstract—3D magnetic resonance imaging (MRI) provides higher image quality but is mainly limited by its long scanning time. k -space undersampling was used to accelerate the acquisition of MRI but always suffer from poorly reconstructed MR images. Recently, some studies 1) used effective undersampling patterns, or 2) designed deep neural networks to improve the image reconstruction from k -space. However, these studies considered undersampling and reconstruction as two separate optimization strategies though they are entangled in theory. In this study, we propose a cross-domain network for MR image reconstruction to simultaneously obtain the optimal undersampling pattern (in k -space under the Cartesian undersampling) and the reconstruction model. The reconstruction model is customized to the type of training data, by using an end-to-end learning strategy. In this model, a 1D probabilistic undersampling layer was designed to obtain the optimal undersampling pattern and its probability distribution in a differentiable way and a 1D inverse Fourier transform layer was implemented to connect the Fourier domain and the image domain during the forward pass and the backpropagation. Finally, by training the network on 3D fully-sampled k -space data and MR images of experimental data with the conventional Euclidean loss, we discover a universal relationship between the probability distribution of the optimal undersampling pattern and its corresponding sampling rate. Retrospective studies with experimental data show that the recovered MRI images using our 1D probabilistic undersampling pattern significantly outperform than those using the existing and start-of-the-art undersampling strategies in both qualitative and quantitative comparison.

Index Terms—Magnetic resonance imaging, undersampling, cross-domain, reconstruction, probability distribution, deep learning.

I. INTRODUCTION

MAGNETIC resonance imaging (MRI) is one of the crucial imaging tools for clinical diagnosis, and fundamental research, due to its non-invasiveness, non-ionizing radiation, and outstanding contrast. Recently, 3D MRI acquisition is becoming popular due to its better performance in image quality and signal-to-noise ratio (SNR) than conventional 1D MRI acquisition. However, the long acquisition time is a primary drawback that limits the applications of 3D

MRI. Parallel imaging relying on the multi-coil technology is useful to accelerate the MRI, but at the cost of hardware requirements. An alternative technique is compressed sensing (CS), because CS overcomes the limitation of the Nyquist-Shannon sampling law with the nature of redundancy in k -space. To this end, recovering a high-quality MR image from its partial undersampled k -space data by using CS becomes feasible without hardware modification. So far, a series of CS-MRI algorithms have been developed, including total variation (TV) [1], k - t FOCUSS [2], nuclear norm [3], [4] and low-rank completion [5]–[8] methods.

Dictionary learning [9] based methods have been used in CS-MRI. However, they have to use numerous iterations and a great deal of time to converge, which can be computationally expensive. This indicates that they are not applicable for large-scale datasets. To this end, deep learning has shown its advantages in CS-MRI reconstruction tasks [13], [15]–[19], [23]–[27], [29]. They obviously reduce the running time of k -space undersampling and reconstruction, and significantly improve the quality of final MR images. These studies design deep neural networks in either the image domain or the Fourier domain. Fig. 1 of [22] provides a thoughtful review of deep learning in CS-MRI.

However, these kinds of methods just take the undersampled partial k -space data as input, and do not consider the undersampling process as one part of the optimization framework. In other words, these studies usually adopt existing undersampling strategies, e.g., Gaussian undersampling or Poisson undersampling. However, it is still unclear whether such undersampling strategy is the best for MRI reconstruction.

Since the model's performance is heavily dependent on the type of undersampling strategy, there are some studies but few focus on optimizing the undersampling patterns to recover high-quality MR images in a data-driven fashion [31]–[34]. However, they have several common drawbacks:

- 1) In application environments, sampling points are binary values and non-differentiable, so that gradient backpropagation cannot be directly applied in the training;
- 2) Integrating the underlying property (rule) of k -space data with the feature extraction capabilities of deep neural networks during training is difficult;
- 3) Optimal undersampling pattern and its corresponding theoretical expression cannot be simultaneously discovered from limited amount of k -space data.

In this study, we propose a cross-domain network for 1D undersampling pattern optimization and MR image reconstruction in a retrospective data-driven fashion and under limited

arXiv:2003.03797v3 [eess.IV] 9 Jan 2022

Corresponding author: Ruiliang Bai (ruiliangbai@zju.edu.cn)

S. Xue and X. Jin are with the College of Information Science and Electronic Engineering, Zhejiang University, Hangzhou, P. R. China (e-mail: xueshengke@zju.edu.cn, jinxy@zju.edu.cn).

R. Bai is with the Department of Physical Medicine and Rehabilitation of the Affiliated Sir Run Run Shaw Hospital AND Interdisciplinary Institute of Neuroscience and Technology, School of Medicine, Zhejiang University, Hangzhou, 310029, China. R. Bai is with the Key Laboratory of Biomedical Engineering of Ministry of Education, College of Biomedical Engineering and Instrument Science, Zhejiang University, Hangzhou, 310029, China (e-mail: ruiliangbai@zju.edu.cn)

Manuscript received **** **, 2020; revised **** **, 2020.

sampling rates (accelerating ratios). The major contributions of this study include:

- We propose a 1D probabilistic undersampling layer including differentiable probability and sampling matrices, to obtain the optimal undersampling pattern and analyze its corresponding probability distribution, which are customized to specific k -space data.
- We propose a 1D inverse Fourier transform layer to achieve the cross-domain scheme. Specifically, the forward pass from the Fourier domain to the image domain and the backpropagation in the inverse direction can be established. To this end, our method simultaneously learns the optimal undersampling pattern (in the Fourier domain) and the corresponding reconstruction model (in the image domain), in an end-to-end training strategy.
- We discover a universal relationship between the probability distribution of our 1D undersampling pattern and its sampling rate, by training limited amount of 3D fully-sampled k -space data and MR images and constrained to the conventional Euclidean loss. Thus, our results can provide theoretical basis for different MRI 3D scanning scenarios.
- Experiments with acquired 3T and 7T MRI data show that, with the same sampling rates, the quantitative and qualitative results of the recovered MR images by our 1D probabilistic undersampling pattern noticeably outperform those by existing state-of-the-art undersampling strategies.

II. METHOD

In this study, the proposed cross-domain framework includes three parts: the 1D probabilistic undersampling layer, the 1D inverse Fourier transform layer, and the reconstruction network.

A. 1D Probabilistic Undersampling Layer

To simulate the process of k -space undersampling in real scenarios, we propose the 1D probabilistic undersampling layer, as shown in Fig. 1, where the input are the fully-sampled k -space data (real and imaginary parts). After undersampling, the output of this layer are the undersampled k -space data, then it can be passed to the next layer. To keep the data format and dimension consistent in training, we separate the real and imaginary parts as two matrices, then concatenate them as two channels:

$$\hat{\mathbf{X}}_{\text{in}} = [\text{real}(\mathcal{K}), \text{imag}(\mathcal{K})] \in \mathbb{R}^{m \times n \times 2}. \quad (1)$$

This strategy [17], [19], [22] can effectively avoid the computation of complex numbers.

In this study, the undersampling process is realized by the Hadamard product, which is respectively applied to the real and imaginary parts, as shown in Fig. 1 and Eq. (2):

$$\begin{aligned} \hat{\mathbf{X}}_{\text{u}} &= \hat{\mathbf{X}}_{\text{in}} \circ \mathbf{M}_{\text{u}} \\ &= [\text{real}(\mathcal{K}) \circ \mathbf{M}_{\text{u}}, \text{imag}(\mathcal{K}) \circ \mathbf{M}_{\text{u}}] \in \mathbb{R}^{m \times n \times 2}, \end{aligned} \quad (2)$$

where “ \circ ” denotes the Hadamard product and $\mathbf{M}_{\text{u}} \in \mathbb{R}^{m \times n}$ denotes the sampling matrix, which has the same dimension

as k -space data and ranges from binary values $\{0, 1\}$. Here, “0” denotes the unused part, shown as the black area in the “mask” of Fig. 1; “1” denotes the sampled part, shown as the white dots in the “mask” of Fig. 1, representing the set of all sampled points in the undersampling pattern. The effect of the Hadamard product is equivalent to preserving partial k -space data by the sampling matrix \mathbf{M}_{u} and discarding other parts, then filled with zeros. To this end, the dimension of output is the same as its input, but with only limited rate of k -space data used. The sampling rate is defined as the number of sampling points in \mathbf{M}_{u} divided by the total number of elements in \mathbf{M}_{u} .

Instead of directly using existing undersampling patterns, we propose a probability matrix, denoted as $\mathbf{P}_{\text{u}} \in \mathbb{R}^{m \times n}$, ranging from the continuous interval $[0, 1]$. By applying the Bernoulli distribution to each element of \mathbf{P}_{u} , we obtain

$$\mathcal{B}(1, p = \mathbf{P}_{\text{u}}(x, y)) = \begin{cases} \mathcal{B}(\mathbf{M}_{\text{u}}(x, y) = 1) = p, \\ \mathcal{B}(\mathbf{M}_{\text{u}}(x, y) = 0) = 1 - p. \end{cases} \quad (3)$$

In this manner, we update each element of \mathbf{M}_{u} by \mathbf{P}_{u} . Every $\mathbf{M}_{\text{u}}(x, y)$ follows the Bernoulli distribution with probability $\mathbf{P}_{\text{u}}(x, y)$, and they are all independently distributed. Similarly, $\mathbf{P}_{\text{u}}(x, y)$ can be considered as the indicator of the importance at the point $\mathbf{M}_{\text{u}}(x, y)$. Thus, only \mathbf{P}_{u} is trainable in our 1D probabilistic undersampling layer. Because the values in \mathbf{M}_{u} are binary (either “0” or “1”) in forward pass, they are natively non-differentiable and have no gradient in backpropagation. Section ?? will provide our solution to this issue.

B. Inverse Fourier Transform Layer

To connect the Fourier domain with the image domain, we design the 1D inverse Fourier transform layer. Since the input of this layer are the undersampled k -space data, we obtain the undersampled MR images via the inverse Fourier transform. The forward and inverse process can be expressed as:

$$\hat{\mathbf{X}}_{\text{u}}(u, v) = \sum_{x=0}^{m-1} \sum_{y=0}^{n-1} \mathbf{X}_{\text{u}}(x, y) e^{-i2\pi(\frac{ux}{m} + \frac{vy}{n})}, \quad (4)$$

$$\mathbf{X}_{\text{u}}(x, y) = \frac{1}{mn} \sum_{u=0}^{m-1} \sum_{v=0}^{n-1} \hat{\mathbf{X}}_{\text{u}}(u, v) e^{i2\pi(\frac{ux}{m} + \frac{vy}{n})}. \quad (5)$$

Note that Eqs. (4) and (5) are dual, except for an extra normalized coefficient $\frac{1}{mn}$ in the inverse transform. It can be seen that every sampling point in k -space contains the global information of an MR image in the image domain. Likewise, each pixel in an MR image is generated by using all k -space data. Eqs. (4) and (5) can be simplified in the matrix form:

$$\mathbf{F}_n = \begin{bmatrix} 1 & 1 & 1 & \cdots & 1 \\ 1 & \omega & \omega^2 & \cdots & \omega^{n-1} \\ \vdots & \vdots & \vdots & \ddots & \vdots \\ 1 & \omega^{n-1} & \omega^{2(n-1)} & \cdots & \omega^{(n-1)(n-1)} \end{bmatrix}, \quad (6)$$

$$\omega = \exp(-i2\pi/n), \quad (7)$$

$$\hat{\mathbf{X}}_{\text{u}} = \mathbf{F}_m \mathbf{X}_{\text{u}} \mathbf{F}_n, \quad (8)$$

$$\mathbf{X}_{\text{u}} = \mathbf{F}_m^{-1} \hat{\mathbf{X}}_{\text{u}} \mathbf{F}_n^{-1} = \frac{1}{mn} \mathbf{F}_m^H \hat{\mathbf{X}}_{\text{u}} \mathbf{F}_n^H, \quad (9)$$

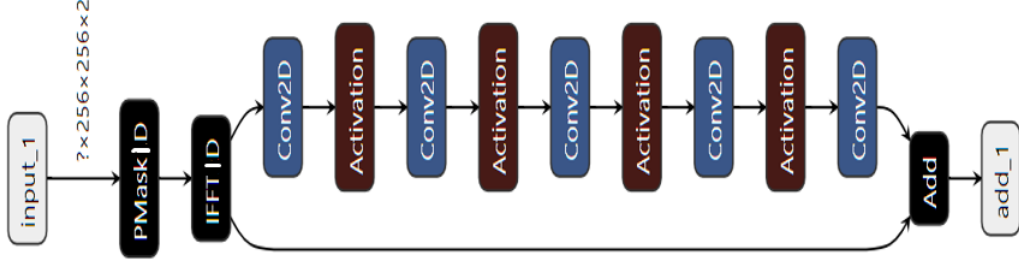


Fig. 1. Overall structure of our proposed cross-domain network: the 1D probabilistic undersampling layer, the inverse Fourier transform layer, and the reconstruction network. Undersampling loss (L_{IFIT}) and reconstruction loss (L_{rec}) are combined for training.

where \mathbf{F}_n is the Fourier matrix and $(\cdot)^{\text{H}}$ denotes the Hermitian transpose. Since the dimension of the Fourier matrix can be preset, \mathbf{F}_m and \mathbf{F}_n are computed in advance and not involved in training. Thus, they are considered as constants and are not required to update. The gradient with respect to the input of the inverse Fourier transform can be expressed as

$$\frac{\partial}{\partial \hat{\mathbf{X}}_u} = \frac{\partial}{\partial \mathbf{X}_u} \frac{\partial \mathbf{X}_u}{\partial \hat{\mathbf{X}}_u} = \frac{1}{mn} \mathbf{F}_m^{\text{H}} \frac{\partial}{\partial \mathbf{X}_u} \mathbf{F}_n^{\text{H}}. \quad (10)$$

Hence, the proposed 1D inverse Fourier transform layer adds a little computational cost. Since we have separated the real and imaginary parts in k -space, we can avoid the complex numbers by saving the real and imaginary components of \mathbf{F}_m and \mathbf{F}_n respectively to accelerate the training period.

C. Reconstruction Network

Fig. 1 illustrates the structure of our proposed reconstruction network (RecNet). It is placed after the inverse Fourier transform layer. In this study, we adopt a common CNN structure with a global skip connection:

$$\mathbf{X}_{\text{rec}} = \mathbf{X}_u + f_{\text{cnn}}(\mathbf{X}_u | \theta), \quad (11)$$

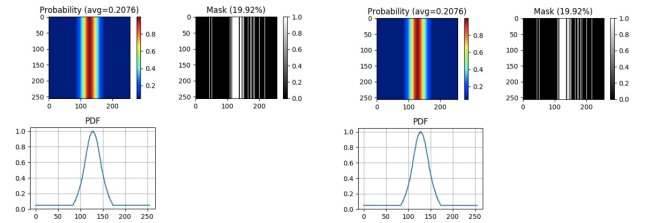
where the depth of CNN is 10, Section IV-A explains how we choose the depth. Except the last convolutional layer (kernel 1×1 , channel = 1, stride = 1, pad = 0) for feature fusion, other convolutional layers have the setting of kernel 3×3 , channel = 16, stride = 1, and pad = 0, followed by the rectified linear unit (ReLU) activation to keep nonlinear capability. The residual learning scheme is adopted to alleviate the gradient vanishing problem, with more details provided in [?]. After training, the output of RecNet \mathbf{X}_{rec} can approximate the ground-truth MR image \mathbf{Y}_{rec} . To obtain the universal results of sampling matrices, we adopt the conventional Euclidean loss to train our model, and this loss is defined as the reconstruction loss:

$$L_{\text{rec}} = \frac{1}{2} \|\mathbf{X}_{\text{rec}} - \mathbf{Y}_{\text{rec}}\|_{\text{F}}^2, \quad (12)$$

where $\|\cdot\|_{\text{F}}$ denotes the Frobenius norm. Unlike other deep learning based MRI reconstruction methods [15]–[19], [23], [24], [29], we focus on discovering and analyzing the undersampling pattern, rather than designing complicated CNN structures.

D. Stable Constraints for Undersampling Patterns

After training, we require stable sampling matrix M_u generated by probability matrix P_u to analyze its pattern. However, randomness from the Bernoulli distribution will interfere at this stage. As shown in Fig. 2a, sampling matrix M_u is generated by probability matrix $P_u = 10\%$ with Bernoulli distribution. It can be seen that those sampling points are randomly placed, where some areas are sparse but others are dense. This makes sampling matrix M_u unstable and difficult to reproduce. Every M_u generated by the same P_u is quite different from each other, so that the performance of the RecNet varies dramatically. This apparently prevents probability matrix P_u from convergence.



(a) 10% sampling matrix with Eq. (13) only (initial status) (b) 20% sampling matrix with Eqs. (13)–(15) (initial status)

Fig. 2. An example of 10% sampling matrices with/out constraints

To overcome the interference caused by randomness, we propose the following stable constraints and they are applied in the stage when probability matrix P_u generates sampling matrix M_u ($P_u \rightarrow M_u$):

1) **Total sampling rate constraint.** During training, the average of the values in probability matrix P_u should be equal to the preset total sampling rate:

$$\|\bar{P}_u - \text{rate}\|_2 < \epsilon, \quad (13)$$

where \bar{P}_u is the average of the probability matrix, $\epsilon = 0.1\%$ is the tolerance and assures that the difference between the actual sampling rate and the preset value is smaller than 0.1%.

2) **Regional sampling distance constraint.** In each region $\mathcal{C} \in \mathbb{R}^{10 \times 10}$, the number of sampling points is allocated according to its probability, i.e., the larger the probability is, the more the sampling points will be. The distances between

those sampling points with the same probability should be nearly uniform, ranging from $[r_0, 2r_0]$. Eqs. (14) and (15) can apparently influence the final pattern in M_u .

$$\left\| \bar{p} - \frac{\sum_{x,y \in C} |M_u(x,y)|}{mn} \right\|_2 < \epsilon, \quad (14)$$

$$r_0 < \|M_u(x_i, y_j) - M_u(x_k, y_l)\|_2 < 2r_0, \quad (15)$$

$$\forall i, k = 1, 2, \dots, m, \quad \forall j, l = 1, 2, \dots, n. \quad (16)$$

where \bar{p} denotes the actual mean value of region $C \in \mathbb{R}^{10 \times 10}$ and r_0 denotes the preset minimal distance of all sampling points. According to Appendix ??, we obtain $\bar{p} = \frac{\sqrt{2}}{10}r_0^2 - \frac{\sqrt{2}}{2}r_0 + 1.0$.

Since the actual sampling distance is integer, distributing sampling points in M_u will bring in some localization error, but we confirm this error is negligible by rigorously assuring that $\|\bar{P}_u - \text{rate}\|_2 < \epsilon$ satisfies.

III. EXPERIMENTS

Our source code is available online¹. It is based on TensorFlow [37] with Keras APIs. Our experiments were executed on a Ubuntu Linux server equipped with an Intel Xeon(R) Platinum CPU @ 2.50 GHz, total 528 GB memory, and four NVIDIA Tesla V100 (32 GB) GPUs. Our 1D probabilistic undersampling strategy was compared with several existing state-of-the-art undersampling methods with sampling rates 10%–50%. The compared undersampling methods are J-CUR [34] (Fig. 3a), PFGMS [31] (Fig. 3b), J-MoDL [33] (Fig. 3c), LOUP [35] (Fig. ??), Gaussian sampling [38] (Fig. ??), and Poisson sampling [39] (Fig. ??). For fair comparison, we replaced our probability and sampling matrices with those compared (either learned or fixed) patterns, and then trained our cross-domain model. As the model parameters trained in different undersampling cases could not be shared, we trained multiple models individually for various sampling rates.

In addition, we aimed to optimize the undersampling pattern and to discover the optimal probability distribution through our 1D probabilistic undersampling layer, rather than to design complicated CNN structures. Consequently, we did not conduct the architecture search for the RecNet.

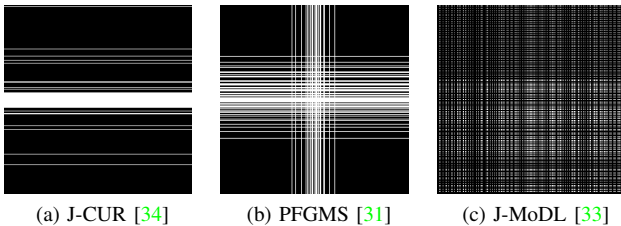


Fig. 3. Several existing k -space undersampling patterns used in this study for comparison

A. Training Configurations and Initialization

At the initial stage of the 1D probabilistic undersampling layer, all values in probability matrix P_u were equal to the

target sampling rate, i.e., $P_u = 10\%$ or 20% . Eq. (13) (i.e., $\bar{P}_u \approx \text{rate}$) was guaranteed during training. The initial status of sampling matrix M_u was decided by probability matrix P_u with Bernoulli distribution. Since each value of probability matrix P_u followed $p \in [0, 1]$, we proposed an upper bound $p \leq P_{\max} = 1$, in case that the probability overflowed. In addition, the Bernoulli distribution made no sense when $p = 0$, since the corresponding values in sampling matrix M_u could not be updated. This led to a local minimum and poor performance of the RecNet. To this end, we proposed a lower bound $p \geq P_{\min}$. Together with the total sampling rate constraint (13), Section IV-D will demonstrate how to decide the precise value of P_{\min} .

Our cross-domain model was trained by using L_{joint} ($\lambda_1 = \lambda_2 = 1$) to analyze the undersampling patterns and compare the quality of final MR images.

The training configurations of our model were summarized in Table I. Some settings of the RecNet have been given in Section II-C. We set the depth of the RecNet as 10, denoted as RecNet-10. Section IV-A will demonstrate how we select the depth of the RecNet.

TABLE I
TRAINING CONFIGURATIONS OF OUR CROSS-DOMAIN MODEL

Description	Value	Description	Value
Batch	16	Optimizer	Adam [36]
Maximal epoch	200	β_1 of Adam	0.9
Initial learning rate	$1e-3$	β_2 of Adam	0.999
Learning policy	Step	Minimal learning rate	$1e-8$
Learning decay	$\sqrt{10}$	Weight decay	$1e-5$
Decay step	20	Device	GPU

B. Datasets

We adopted the 3T MR images from Multi-modal Brain Tumor Segmentation Challenge 2018 [40], [41], as the training and validation sets, denoted as BraTS 2018. All image slices were obtained by 3D scanning. Specifically, it contains 200 training volumes and 50 validation volumes. Each volume comes from one patient/candidate. The spatial resolution is $256 \times 256 \times (240-320)$, the minimal voxel is 1 mm^3 . We chose 200 volumes for training and 10 out of 50 volumes for validation. The pixels' intensity was normalized to $[0, 1]$.

As for the test set, we acquired 3D T1-weighted MRI data (brain only) from healthy volunteers on both 3T (SIEMENS Prisma) and 7T (SIEMENS Magnetom) scanners, denoted as Test3T&7T. Here both the fully-sampled k -space data (Cartesian sampling) and MR images were obtained and kept. It consists of 20 volumes of k -space data from 10 different volunteers. Each one was scanned in both 3T and 7T MRI. The spatial resolutions are $256 \times 256 \times 192$ for 3T and $310 \times 314 \times 208$ for 7T, respectively. We used MRI data from two-field MRI scanners with different resolutions to prove the generalization of our proposed method.

Since we focused on the human tissue and ignored the background in MR images, we proposed the following data argumentation strategy:

¹<https://github.com/xueshengke/1D-PUPO>

- 1) **Translation.** All contents of tissue were translated to the geometrical center of MR images.
- 2) **Rotation.** All images were randomly rotated $[0, 360)$ degrees by 8 times.

This strategy was used to prevent the over-fitting problem and boosted the generalization capability of our model. Because most of images in BraTS 2018 are similar and have fixed shapes, the diversity of k -space data is obviously insufficient. To obtain the universal probabilistic undersampling patterns after training, our data argumentation strategy (translation and random rotation) significantly enriches the diversity of our training set. Section IV-D shows that our probability matrices trained with various sampling rates are perfectly symmetric.

To keep the dimension of training data consistent, we resized all MR images to 256×256 and concatenated them along the sagittal direction. Thus, during training and validation, the dimension of one batch became $256 \times 256 \times N$, where N is the batch size.

Since the k -space data were used as the input of our model while BraTS 2018 only provided MR images, we converted all training and validation images into the frequency domain via the 1D fast Fourier transform. As for the test set, we directly used 3T/7T fully-sampled k -space data. To avoid complex values, we split the real and imaginary parts, then combined them as two channels. The MR images reconstructed from fully-sampled k -space data in training and test sets were used as the ground-truth.

C. Evaluation Metric

Peak signal-to-noise ratio (PSNR) has been commonly used to measure the quality of MR images in various computer vision tasks. PSNR is defined as follows:

$$\text{MSE} = \frac{1}{N} \|\mathbf{I}_{\text{rec}} - \mathbf{I}_{\text{gnd}}\|_{\text{F}}^2, \quad (17)$$

$$\text{PSNR} = 10 \cdot \log_{10} \left(\frac{P_{\text{max}}^2}{\text{MSE}} \right) \text{ dB}, \quad (18)$$

where \mathbf{I}_{rec} is the recovered image, \mathbf{I}_{gnd} is the original image, and P_{max} is the maximum pixel value (normally 1.0) of an image. A high-quality MR image usually has a large value of PSNR and a lower value of mean-squared error (MSE). Although structural similarity index (SSIM) [42] is often adopted to evaluate the quality of MR images, we found that the most values of SSIM of recovered MR images were nearly equal to 1.0, which were too difficult to distinguish. Thus, we used only PSNR as the effective metric to evaluate the performances of different methods.

In our model, we adopted two loss functions: undersampling loss L_{IFT} and reconstruction loss L_{rec} , for supervised training. Correspondingly, we presented two indicators: undersampling PSNR (\mathbf{X}_{u} vs. \mathbf{Y}_{rec}) and reconstruction PSNR (\mathbf{X}_{rec} vs. \mathbf{Y}_{rec}).

IV. RESULTS AND DISCUSSIONS

A. Effect of Reconstruction Network

Table II shows the PSNR of our 1D probabilistic undersampling layer with different depths of RecNet and sampling rate 10%–50%. These results were obtained from the Test3T&7T

TABLE II
PSNR OF OUR 1D PROBABILISTIC UNDERSAMPLING LAYER WITH VARIOUS DEPTHS OF RECNET AND SAMPLING RATE 10%–50%. RESULTS WERE OBTAINED FROM THE TEST3T&7T SET

Sampling rate	Undersampling PSNR (dB) / Reconstruction PSNR (dB)				
	RecNet-0	RecNet-5	RecNet-10	RecNet-15	RecNet-20
10.09%	32.80 / -	33.03 / 36.43	34.25 / 37.34	34.99 / 38.08	35.33 / 38.74
20.01%	34.98 / -	35.67 / 38.49	36.83 / 39.15	36.99 / 39.87	37.68 / 40.09
29.91%	36.06 / -	37.01 / 40.91	38.70 / 41.46	39.04 / 42.34	39.63 / 42.97
40.04%	37.14 / -	39.49 / 41.99	40.99 / 43.87	41.51 / 44.13	42.03 / 44.55
50.00%	39.56 / -	41.32 / 44.56	42.01 / 45.92	42.51 / 46.21	43.36 / 46.36

Note: -0 for no RecNet; -5, -10, -15, -20 for the depths of the RecNet

set. It can be seen that the difference between the actual sampling rate and the target value is quite small ($<0.1\%$), which proves the effectiveness of our total sampling rate constraint (13). As the sampling rate or the depth of RecNet increases, the undersampling PSNR and reconstruction PSNR both improve significantly. Note that the improvement first comes from our 1D probabilistic undersampling patterns, then from our trained RecNet. The deeper the RecNet is, the better the quality of MR images we can obtain. In addition, when the sampling rates are identical, the undersampling PSNR also improves with the increasing of the depth of RecNet, which indicates that our cross-domain training scheme can simultaneously optimize the 1D probabilistic undersampling layer and the RecNet, and obtain matched sampling matrices and parameters of RecNet.

Fig. 4 shows the number (#) of parameters and floating operations per second (flops) of our 1D probabilistic undersampling layer with different depths of the RecNet. These results were based on the BraTS 2018 training set. Most parameters are in the probability matrix and sampling matrix of our 1D probabilistic undersampling layer, i.e., $256 \times 256 \times 2 = 131,072$. In the RecNet, only a few parameters exist. However, as the depth of RecNet increases, the number of flops rises rapidly, because the feature maps with the size of 256×256 require a huge amount of computational cost in convolution. To balance the performance and computational burden of our model, we chose the depth as 10 in the rest of experiments.

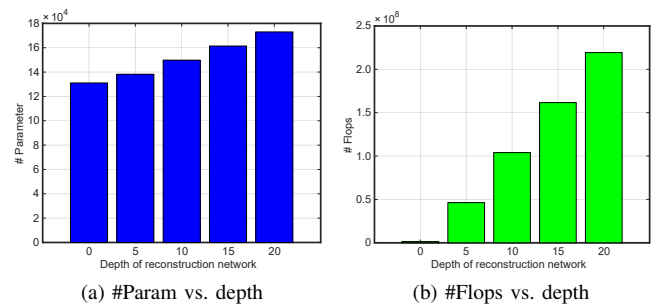


Fig. 4. #Param and #Flops of our 1D probabilistic undersampling layer with different depths of RecNet obtained from the BraTS 2018 training set

B. Effect of Stable Constraints

Fig. 5 shows the sampling matrices of our 1D probabilistic undersampling layer by sampling rate 10.05% with Eq. (13)

and Eqs. (13)–(15), respectively. As shown in Fig. 5a, the sampling points in k -space are distributed randomly since no regional sampling distance constraints (14) and (15) are used. Especially in the high-frequency (HF) area, those sampling points generated by the Bernoulli distribution are either too sparse or too dense, though their probability values are the same. This apparently prevents us from analyzing its probability distribution. As shown in Fig. 5b, those sampling points in k -space are uniformly distributed by adopting (14) and (15), especially in the HF area. This intuitively indicates that the probability values are equal in that area. In addition, after integrating the regional sampling distance constraint, the sampling matrices are quite stable and repeatable even through multiple trials.

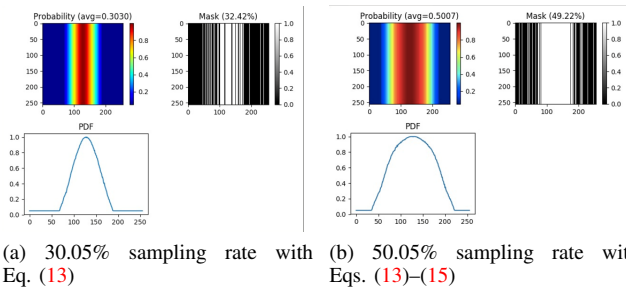


Fig. 5. Sampling matrices of our 1D probabilistic undersampling layer by sampling rate 10.05% with Eq. (13) and Eqs. (13)–(15) respectively

Fig. 6a shows the PSNR of our 1D probabilistic undersampling layer (no RecNet) using the total sampling rate constraint only or together with the regional sampling distance constraint, respectively. The results were based on the Test3T&7T set with sampling rate 10%–50%. It can be seen that the regional sampling distance constraint not only helps generate stable sampling matrices, but also improves the undersampling PSNR of MR images by nearly 0.8–2.8 dB. Fig. 6b shows the PSNR of our 1D probabilistic undersampling layer (with RecNet-10) using the total sampling rate constraint only or together with the regional sampling distance constraint, respectively. With the advantage of RecNet-10, our method can further improve the PSNR of final MR images by nearly 0.7–2.1 dB. Fig. 6 shows that the stable constraints and RecNet-10 both effectively improve the PSNR of our cross-domain model.

The total sampling rate constraint ensures that the difference between the actual sampling rate and the target value is smaller than 0.1%. This is convenient for us to analyze the relationship between the sampling matrix and the sampling rate. Thus, in the rest of experiments, we adopted the total sampling rate constraint and regional sampling distance constraint together (known as stable constraints), to obtain stable sampling matrices and substantially improve the PSNR of final MR images.

C. Comparison of Different Undersampling Patterns

Table III compares the PSNR values from different undersampling methods (with RecNet-10) based on Test3T&7T set with sampling rate 10%–50%. As the sampling rate increases, the PSNR values of all methods improve gradually. It can be seen that the undersampling patterns of J-CUR and PFGMS

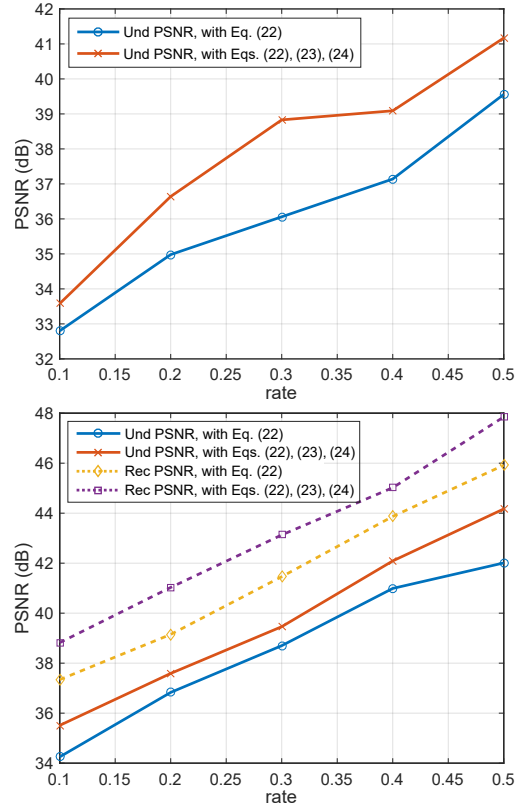


Fig. 6. PSNR of our cross-domain model using the total sampling rate constraint only (Eq. (13)) or together with the regional sampling distance constraint (Eqs. (13)–(15)), respectively. The results were obtained from the Test3T&7T set with sampling rate 10%–50%: (a) undersampling PSNR without RecNet; (b) undersampling / reconstruction PSNR with RecNet-10

perform worse than others, where the J-CUR only samples in 1D phase encoding direction and ignores the other dimension, as shown in Fig. 3a. Since PFGMS allocates most sampling lines in the LF area, as shown in Fig. 3b, its PSNR value is slightly better than J-CUR. Their common disadvantage is that the majority of HF information is lost, leading to low-quality of MR images. J-MoDL trains both the deep network and 1D undersampling pattern, but it samples evenly in the LF and HF areas, as shown in Fig. 3c, so that its PSNR value is within 2.3 dB better than the two methods mentioned above. This indicates that the improvement of the undersampling pattern by J-MoDL is still limited. However, the undersampling pattern of LOUP, which is symmetric in Fig. ??, properly allocates the sampling points in LF and HF areas. Thus, it obviously improves the PSNR of recovered images. In addition, by using 1D probability functions, Gaussian and Poisson undersampling patterns have similar PSNR values and both outperform aforementioned methods. As a result, our proposed probabilistic undersampling pattern, integrated with RecNet-10, can obtain 2–3 dB higher values of PSNR than Gaussian and Poisson undersampling methods, under various sampling rates. Unlike other sampling patterns, our probability matrix can accurately control the status of each sampling point, and our sampling matrix only requires random initialization. By jointly cross-domain training the undersampling pattern and RecNet, our method can effectively obtain the best PSNR of the recovered

TABLE III
COMPARISON OF PSNR BY VARIOUS UNDERSAMPLING METHODS (WITH RECNET-10). RESULTS WERE BASED ON TEST3T&7T SET WITH SAMPLING RATE 10%–50%

Sampling rate	Undersampling PSNR (dB) / Reconstruction PSNR (dB)						
	J-CUR [34]	PFGMS [31]	J-MoDL [33]	LOUP [35]	Gaussian [38]	Poisson [39]	Probabilistic
10.09%	27.23 / 30.85	29.51 / 31.02	30.19 / --	31.48 / 34.21	33.08 / 36.34	33.21 / 36.95	35.51 / --
20.01%	29.46 / 31.34	31.35 / 33.24	32.37 / --	33.76 / 36.85	35.39 / 39.30	35.26 / 39.13	37.59 / --
29.91%	30.54 / 32.83	32.48 / 35.91	33.89 / --	35.30 / 38.76	37.27 / 41.06	37.53 / 41.44	39.46 / --
40.04%	31.09 / 33.15	33.72 / 37.67	35.64 / --	37.49 / 39.97	39.31 / 41.83	39.22 / 42.00	42.09 / --
50.00%	32.64 / 34.79	35.83 / 39.67	37.28 / --	38.65 / 41.40	40.20 / 43.15	40.42 / 43.66	44.17 / --

MR images.

Fig. 7 shows an example of comparison in recovered MR images from different undersampling methods (with RecNet-10) based on the Test7T set with sampling rate 20%. It can be seen that the recovered MR images by the J-CUR and PFGMS methods are quite blurry, and some details have been lost in the undersampling process. By increasing the sampling rate in the HF area, J-MoDL method obviously improves the PSNR of final results. However, its improvement is fairly limited, because J-MoDL deals with the LF and HF areas evenly, by allocating nearly identical sampling rates. In contrast, the LOUP method has most sampling points in the LF area and keeps a small number of sampling points randomly in the HF area, which apparently recovers small fine structures in MR images. In addition, by generating from 1D probability functions, the Gaussian and Poisson undersampling methods accurately distribute every sampling point in k -space, which significantly reconstructs sophisticated structures and improves the quality of MR images. Our proposed 1D probabilistic undersampling pattern, trained with RecNet-10 on fully-sampled k -space data, distributes those sampling points in LF and HF areas by using the probability values. Thus, our method can effectively obtain higher PSNR values of MR images with more fine structures reconstructed than all other methods (red arrow in Fig. 7).

D. Analysis of 1D Probabilistic Undersampling Pattern

To be continued ...

V. CONCLUSION

In this paper, we have proposed a cross-domain network for MR image reconstruction, which contains a 1D probabilistic undersampling layer, a 1D inverse Fourier transform layer, and a reconstruction network. We can simultaneously obtain the optimal undersampling pattern (in k -space) and the reconstruction model. The 1D probabilistic undersampling layer, with differentiable probability and sampling matrices, can generate the optimal undersampling pattern and its probability distribution customized to specific k -space data. The 1D inverse Fourier transform layer connects the Fourier domain and the image domain during the forward pass and backpropagation. By training 3D fully-sampled k -space data and MR images with the conventional Euclidean loss, we have discovered the universal relationship between the probability function of the optimal undersampling pattern (sampling matrix) and its

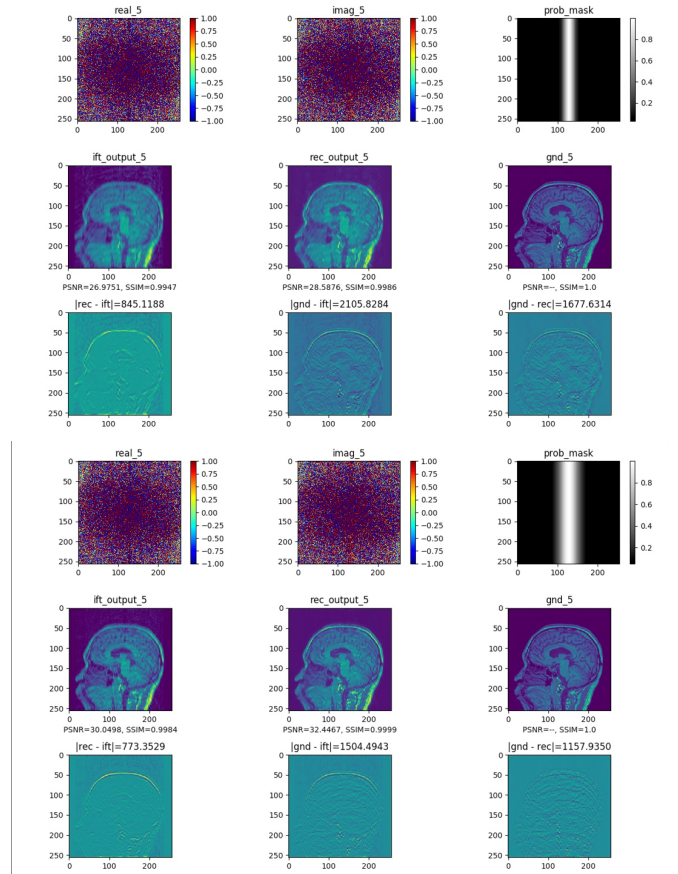


Fig. 7. An example of comparison in recovered MR images resulting from different undersampling methods (with RecNet-10) based on the Test7T set with sampling rate 20%: (a) Original; (b) J-CUR; (c) PFGMS; (d) J-MoDL; (e) LOUP; (f) Gaussian; (g) Poisson; (h) Probabilistic. Probabilistic undersampling method shows the best performance in reconstructing fine anatomic structures. The corresponding PSNR were labeled for each method.

target sampling rate. Retrospective experiments verify that the quality of recovered MR images by our 1D probabilistic undersampling pattern is apparently better than those by existing undersampling methods.

REFERENCES

- [1] S. Osher, M. Burger, D. Goldfarb, J. Xu, and W. Yin, "An iterative regularization method for total variation-based image restoration," *Multiscale Modeling & Simulation*, vol. 4, no. 2, pp. 460–489, 2005.
- [2] H. Jung, J. Yoo, and J. Ye, "Generalized k-t BLAST and k-t SENSE using FOCUSS," in *IEEE 4th International Symposium on Biomedical Imaging*. IEEE, 2007, pp. 145–148.

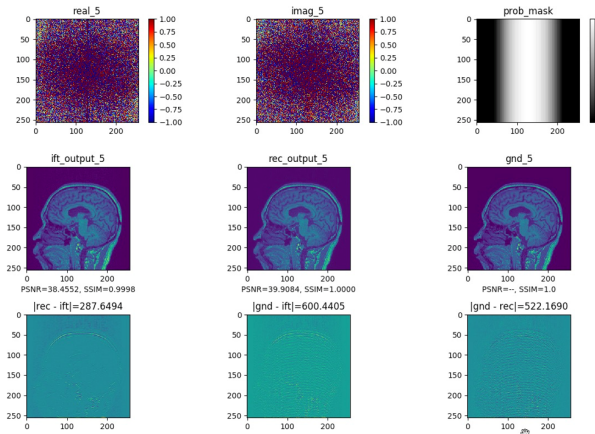


Fig. 9. An example of comparison in recovered MR images resulting from different undersampling methods (with RecNet-10) based on the Test7T set with sampling rate 20%: (a) Original; (b) J-CUR; (c) PFGMS; (d) J-ModL; (e) LOUP; (f) Gaussian; (g) Poisson; (h) Probabilistic. Probabilistic undersampling method shows the best performance in reconstructing fine anatomic structures. The corresponding PSNR were labeled for each method.

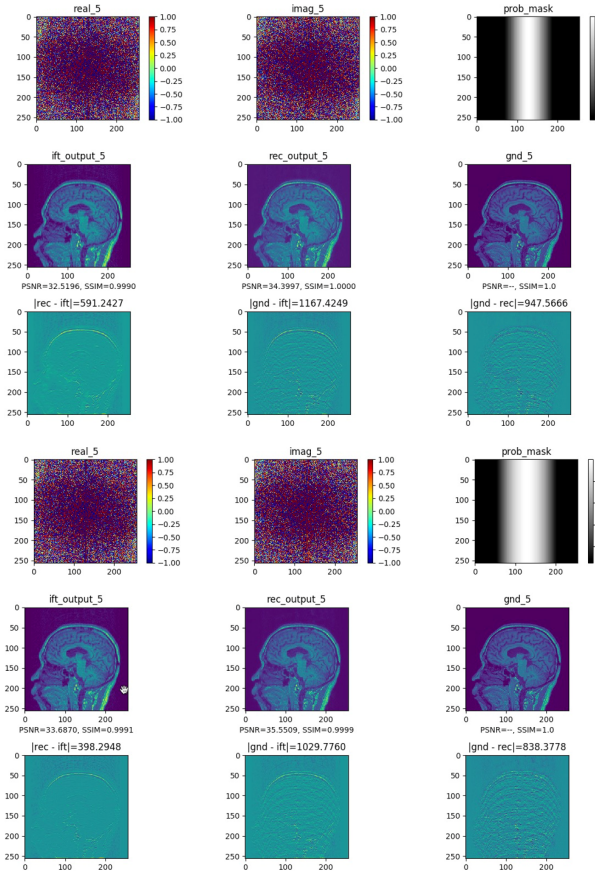


Fig. 8. An example of comparison in recovered MR images resulting from different undersampling methods (with RecNet-10) based on the Test7T set with sampling rate 20%: (a) Original; (b) J-CUR; (c) PFGMS; (d) J-ModL; (e) LOUP; (f) Gaussian; (g) Poisson; (h) Probabilistic. Probabilistic undersampling method shows the best performance in reconstructing fine anatomic structures. The corresponding PSNR were labeled for each method.

[3] G. Ongie and M. Jacob, "A fast algorithm for structured low-rank matrix recovery with applications to undersampled MRI reconstruction," in *IEEE 13th International Symposium on Biomedical Imaging (ISBI)*. Prague: IEEE, apr 2016, pp. 522–525.

- [4] L. Sun, J. Chen, D. Zeng, and X. Ding, "A novel nonlocal MRI reconstruction algorithm with patch-based low rank regularization," in *IEEE Global Conference on Signal and Information Processing*. IEEE, dec 2015, pp. 398–402.
- [5] E. J. Candes, X. Li, Y. Ma, and J. Wright, "Robust principal component analysis," *Journal of the ACM*, vol. 58, no. 3, p. 11, 2011.
- [6] J. Wright, A. Ganesh, S. Rao, Y. Peng, and Y. Ma, "Robust principal component analysis: exact recovery of corrupted low-rank matrices via convex optimization," in *Advances in Neural Information Processing Systems*, 2009, pp. 2080–2088.
- [7] S. Xue, W. Qiu, F. Liu, and X. Jin, "Low-rank tensor completion by truncated nuclear norm regularization," in *24th International Conference on Pattern Recognition (ICPR)*. Beijing, China: IEEE, aug 2018, pp. 2600–2605.
- [8] S. Xue and X. Jin, "Robust classwise and projective low-rank representation for image classification," *Signal, Image and Video Processing*, vol. 12, no. 1, pp. 107–115, jan 2018.
- [9] M. Aharon, M. Elad, and A. Bruckstein, "K-SVD: an algorithm for designing overcomplete dictionaries for sparse representation," *IEEE Transactions on Signal Processing*, vol. 54, no. 11, pp. 4311–4322, 2006.
- [10] M. Manimala, C. Naidu, and M. N. Giriprasad, "Sparse recovery algorithms based on dictionary learning for MR image reconstruction," in *International Conference on Wireless Communications, Signal Processing and Networking*. IEEE, mar 2016, pp. 1354–1360.
- [11] S. Ravishanker and Y. Bresler, "MR image reconstruction from highly undersampled k-space data by dictionary learning," *IEEE Transactions on Medical Imaging*, vol. 30, no. 5, pp. 1028–1041, 2011.
- [12] H. Bristow, A. Eriksson, and S. Lucey, "Fast convolutional sparse coding," in *IEEE Conference on Computer Vision and Pattern Recognition*, S. Ourselin, L. Joskowicz, M. R. Sabuncu, G. Unal, and W. Wells, Eds. Cham: IEEE, jun 2013, pp. 391–398.
- [13] L. Sun, Z. Fan, Y. Huang, X. Ding, and J. Paisley, "Compressed sensing MRI using a recursive dilated network," in *32nd AAAI Conference on Artificial Intelligence*, 2017, pp. 2444–2451.
- [14] D. Lee, J. Yoo, S. Tak, and J. C. Ye, "Deep residual learning for accelerated MRI using magnitude and phase networks," *IEEE Transactions on Biomedical Engineering*, vol. 65, no. 9, pp. 1985–1995, sep 2018.
- [15] C. M. Hyun, H. P. Kim, S. M. Lee, S. Lee, and J. K. Seo, "Deep learning for undersampled MRI reconstruction," *Physics in Medicine and Biology*, vol. 63, no. 13, p. 135007, 2018.
- [16] G. Yang, S. Yu, H. Dong, G. Slabaugh, P. L. Dragotti, X. Ye, F. Liu, S. Arridge, J. Keegan, Y. Guo, and D. Firmin, "DAGAN: deep de-aliasing generative adversarial networks for fast compressed sensing MRI reconstruction," *IEEE Transactions on Medical Imaging*, vol. 37, no. 6, pp. 1310–1321, jun 2018.
- [17] T. M. Quan, T. Nguyen-Duc, and W. K. Jeong, "Compressed sensing MRI reconstruction using a generative adversarial network with a cyclic loss," *IEEE Transactions on Medical Imaging*, vol. 37, no. 6, pp. 1488–1497, 2018.
- [18] S. Wang, Z. Su, L. Ying, X. Peng, S. Zhu, F. Liang, D. Feng, and D. Liang, "Accelerating magnetic resonance imaging via deep learning," in *International Symposium on Biomedical Imaging*. IEEE, 2016, pp. 514–517.
- [19] J. Schlemper, J. Caballero, J. V. Hajnal, A. Price, and D. Rueckert, "A deep cascade of convolutional neural networks for MR image reconstruction," in *International Conference on Information Processing in Medical Imaging*, M. Niethammer, M. Styner, S. Aylward, H. Zhu, I. Oguz, P.-T. Yap, and D. Shen, Eds. Cham: Springer International Publishing, 2017, pp. 647–658.
- [20] B. Zhu, J. Z. Liu, S. F. Cauley, B. R. Rosen, and M. S. Rosen, "Image reconstruction by domain-transform manifold learning," *Nature*, vol. 555, no. 7697, pp. 487–492, 2018.
- [21] I. Oksuz, J. Clough, A. Bustin, G. Cruz, C. Prieto, R. Botnar, D. Rueckert, J. A. Schnabel, and A. P. King, "Cardiac MR motion artefact correction from k-space using deep learning-based reconstruction," in *International Workshop on Machine Learning for Medical Image Reconstruction*, F. Knoll et al., Ed. Springer, 2018, pp. 21–29.
- [22] Y. Han, L. Sunwoo, and J. C. Ye, "k-space deep learning for accelerated MRI," *IEEE Transactions on Medical Imaging*, vol. 39, no. 2, pp. 377–386, feb 2020.
- [23] J. Zhang and B. Ghanem, "ISTA-Net: interpretable optimization-inspired deep network for image compressive sensing," in *IEEE Conference on Computer Vision and Pattern Recognition*, 2018, pp. 1828–1837.
- [24] S. Pereira, A. Pinto, V. Alves, and C. A. Silva, "Brain tumor segmentation using convolutional neural networks in MRI images," *IEEE Transactions on Medical Imaging*, vol. 35, no. 5, pp. 1240–1251, 2016.

- [25] H.-C. Shin, H. R. Roth, M. Gao, L. Lu, Z. Xu, I. Noguees, J. Yao, D. Mollura, and R. M. Summers, "Deep convolutional neural networks for computer-aided detection: CNN architectures, dataset characteristics and transfer learning," *IEEE Transactions on Medical Imaging*, vol. 35, no. 5, pp. 1285–1298, 2016.
- [26] K. Bahrami, F. Shi, X. Zong, H. W. Shin, H. An, and D. Shen, "Reconstruction of 7T-like images from 3T MRI," *IEEE Transactions on Medical Imaging*, vol. 35, no. 9, pp. 2085–2097, 2016.
- [27] Y. Yang, J. Sun, H. Li, and Z. Xu, "ADMM-Net: a deep learning approach for compressive sensing MRI," *arXiv Preprint*, vol. 1705.06869, pp. 1–14, 2017.
- [28] O. Ronneberger, P. Fischer, and T. Brox, "U-Net: convolutional networks for biomedical image segmentation," in *International Conference on Medical Image Computing and Computer-Assisted Intervention*, N. Navab, J. Hornegger, W. M. Wells, and A. F. Frangi, Eds. Cham: Springer International Publishing, 2015, pp. 234–241.
- [29] M. Mardani, E. Gong, J. Y. Cheng, S. S. Vasanawala, G. Zaharchuk, L. Xing, and J. M. Pauly, "Deep generative adversarial neural networks for compressive sensing (GANCS) MRI," *IEEE Transactions on Medical Imaging*, vol. 38, no. 1, pp. 167–179, jan 2019.
- [30] J.-Y. Zhu, T. Park, P. Isola, and A. A. Efros, "Unpaired image-to-image translation using cycle-consistent adversarial networks," in *IEEE International Conference on Computer Vision*. IEEE, oct 2017, pp. 2242–2251.
- [31] B. Gözcü, R. K. Mahabadi, Y.-H. Li, E. Ilıcak, T. Cukur, J. Scarlett, and V. Cevher, "Learning-based compressive MRI," *IEEE Transactions on Medical Imaging*, vol. 37, no. 6, pp. 1394–1406, jun 2018.
- [32] I. A. Huijben, B. S. Veeling, and R. J. van Sloun, "Deep probabilistic subsampling for task-adaptive compressed sensing," in *International Conference for Learning Representations*, 2020, pp. 1–16.
- [33] H. K. Aggarwal and M. Jacob, "J-MoDL: joint model-based deep learning for optimized sampling and reconstruction," *arXiv Preprint*, vol. 1911.02945, pp. 1–10, 2019.
- [34] T. Weiss, S. Vedula, O. Senouf, O. Michailovich, M. Zibulevsky, and A. Bronstein, "Joint learning of Cartesian under sampling andre construction for accelerated MRI," in *IEEE International Conference on Acoustics, Speech and Signal Processing (ICASSP)*. IEEE, may 2020, pp. 8653–8657.
- [35] C. D. Bahadir, A. V. Dalca, and M. R. Sabuncu, "Learning-based optimization of the undersampling pattern in MRI," in *International Conference on Information Processing in Medical Imaging*, vol. 12, no. 6. Springer, 2019, pp. 780–792.
- [36] D. P. Kingma and J. Ba, "Adam: a method for stochastic optimization," in *International Conference for Learning Representations*, San Diego, dec 2015, pp. 1–13.
- [37] M. Abadi, P. Barham, J. Chen, Z. Chen, A. Davis, and J. Dean, "Tensorflow: A system for large-scale machine learning," in *12th USENIX Symposium on Operating Systems Design and Implementation (OSDI)*, 2016, pp. 265–283.
- [38] R. L. Cook, "Stochastic sampling in computer graphics," *ACM Transactions on Graphics (TOG)*, vol. 5, no. 1, pp. 51–72, jan 1986.
- [39] T. R. Jones, "Efficient generation of Poisson-disk sampling patterns," *Journal of Graphics Tools*, vol. 11, no. 2, pp. 27–36, jan 2006.
- [40] L. Liu, G. Zheng, J. D. Bastian, M. J. B. Keel, L. P. Nolte, K. A. Siebenrock, and T. M. Ecker, "Periacetabular osteotomy through the pararectus approach: technical feasibility and control of fragment mobility by a validated surgical navigation system in a cadaver experiment," *International Orthopaedics*, vol. 40, no. 7, pp. 1389–1396, jul 2016.
- [41] S. Bakas, H. Akbari, A. Sotiras, M. Bilello, M. Rozycki, J. S. Kirby, J. B. Freymann, K. Farahani, and C. Davatzikos, "Advancing the cancer genome atlas glioma MRI collections with expert segmentation labels and radiomic features," *Scientific Data*, vol. 4, p. 170117, sep 2017.
- [42] Z. Wang, A. Bovik, H. Sheikh, and E. Simoncelli, "Image quality assessment: from error visibility to structural similarity," *IEEE Transactions on Image Processing*, vol. 13, no. 4, pp. 600–612, apr 2004.